

Ionic Mechanisms in the Generation of Subthreshold Oscillations and Action Potential Clustering in Entorhinal Layer II Stellate Neurons

Erik Fransén,^{1*} Angel A. Alonso,² Clayton T. Dickson,³ Jacopo Magistretti,⁴
and Michael E. Hasselmo⁵

ABSTRACT: A multicompartamental biophysical model of entorhinal cortex layer II stellate cells was developed to analyze the ionic basis of physiological properties, such as subthreshold membrane potential oscillations, action potential clustering, and the medium afterhyperpolarization. In particular, the simulation illustrates the interaction of the persistent sodium current (I_{NaP}) and the hyperpolarization activated inward current (I_h) in the generation of subthreshold membrane potential oscillations. The potential role of I_h in contributing to the medium hyperpolarization (mAHP) and rebound spiking was studied. The role of I_h and the slow calcium-activated potassium current $I_{K(AHP)}$ in action potential clustering was also studied. Representations of I_h and I_{NaP} were developed with parameters based on voltage-clamp data from whole-cell patch and single channel recordings of stellate cells (Dickson et al., *J Neurophysiol* 83:2562–2579, 2000; Magistretti and Alonso, *J Gen Physiol* 114:491–509, 1999; Magistretti et al., *J Physiol* 521:629–636, 1999a; *J Neurosci* 19:7334–7341, 1999b). These currents interacted to generate robust subthreshold membrane potentials with amplitude and frequency corresponding to data observed in the whole cell patch recordings. The model was also able to account for effects of pharmacological manipulations, including blockade of I_h with ZD7288, partial blockade with cesium, and the influence of barium on oscillations. In a model with a wider range of currents, the transition from oscillations to single spiking, to spike clustering, and finally tonic firing could be replicated. In agreement with experiment, blockade of calcium channels in the model strongly reduced clustering. In the voltage interval during which no data are available, the model predicts that the slow component of I_h does not follow the fast component down to very short time constants. The model also predicts that the fast component of I_h is responsible for the involvement in the generation of subthreshold oscillations, and the slow component dominates in the generation of spike clusters. © 2004 Wiley-Liss, Inc.

KEY WORDS: biophysical modeling; subthreshold oscillation; spike clustering; medium afterhyperpolarization; entorhinal cortex

¹Department of Numerical Analysis and Computer Science, Royal Institute of Technology, Stockholm, Sweden; ²Department of Neurology and Neurosurgery, Montreal Neurological Institute and McGill University, Montreal, Canada; ³Department of Psychology, University of Alberta, Edmonton, Canada; ⁴Department of Physiological and Pharmacological Sciences, University of Pavia, Pavia, Italy; ⁵Department of Psychology, Boston University, Boston, Massachusetts

Grant sponsor: Swedish Foundation for International Cooperation in Research and Higher Education (STINT); Grant number: 97/248. Grant sponsor: P.E. Lindahls Fund; Grant sponsor: The Swedish Research Council; Grant number: 240-00023-061; Grant sponsor: Human Frontier Science Program; Grant sponsor: National Institute of Mental Health (NIMH); Grant number: 61492; Grant sponsor: National Institutes of Health (NIH); Grant number MH61492; Grant number: MH60013.

*Correspondence to: Erik Fransén, Department of Numerical Analysis and Computer Science, Royal Institute of Technology, SE-100 44 Stockholm, Sweden. E-mail: erikf@nada.kth.se

Accepted for publication 10 July 2003

DOI 10.1002/hipo.10198

Published online to come 2004 in Wiley InterScience (www.interscience.wiley.com).

INTRODUCTION

In this work, biophysical modeling is used to study the ionic basis of salient electroresponsive properties of layer II stellate cells (SCs), such as subthreshold membrane potential oscillations (MPOs), action potential clustering and the medium afterhyperpolarization (mAHP) (Klink and Alonso, 1993). We show how these physiological properties of SCs could strongly depend on a hyperpolarization activated cation current I_h . In particular, the role of this current in the generation of MPOs was analyzed because it has been shown in SCs that the I_h , rather than a slow potassium conductance, is critically involved in the repolarizing phase of the oscillation (Dickson et al., 2000), and h-channels are highly abundant in SCs (Alonso and Llinas, 1989; Dickson et al., 2000; Vasilyev and Barish, 2002). Further, clustering is known to depend on a calcium influx (Klink and Alonso, 1993), presumably affecting a Ca-dependent potassium current. However, the residual clustering remaining after a Ca-conductance block (Klink and Alonso, 1993) is shown to be due potentially to I_h deactivation. Simulation of these physiological properties in detailed compartmental simulations is an important step in investigating their role in network dynamics.

A number of different currents have been proposed to play a role in subthreshold MPOs in different neuronal populations (Alonso and Llinas, 1989; Wang, 1993; Gutfreund et al., 1995; Pape et al., 1998), but different neuronal subtypes appear to show subthreshold oscillations, depending on different sets of currents. Most previous work on subthreshold oscillations in entorhinal cortex stellate neurons (Wang, 1993; White et al., 1995, 1998) has focused on a potential interaction between a persistent sodium current and an outward rectifier. However, recent experimental data (Dickson and Alonso, 1998; Dickson et al., 2000), modeling work (Fransén et al., 1998; Dickson et al., 2000), and the present modeling analysis suggest that interactions between the persistent sodium current and the hyperpolarization activated inward current (I_h) are the crucial elements for the generation of MPOs in these neurons. The biophysical simulations we now present provide a detailed analysis of this potential role of I_h in generating subthreshold oscillations.

A hyperpolarization-activated nonselective cationic current has been described in a number of different cell

types, including cardiac pacemaker cells (DiFrancesco et al., 1986), where it is termed I_f as well as a rich diversity of brain neurons (Pape, 1996) and thalamic neurons (McCormick and Pape, 1990). While these different currents share a common profile of activation, causing a depolarizing “sag” of the membrane potential during the later stages of a hyperpolarizing current injection, several differences in the gating of these currents are evident in different neuronal subtypes, and they are related to the expression of different h-channel subtypes (Ludwig et al., 1998; Santoro et al., 1998). Significantly, native h-currents exhibit greater diversity in their gating behavior than the different h-channels isoforms, when expressed in heterologous cells (Robinson and Siegelbaum, 2003) caused by the expression of different h-channel subtypes (Santoro et al., 2000). Therefore, a number of models of the h-current have been presented based on experimental work in a variety of cell types. Using a model of the steady-state activation and the activation time constant, voltage-clamp and current-clamp simulations have been carried out for neurons of the rat sensorimotor cortex (Spain et al., 1987; Hutcheon et al., 1996a,b), and thalamic relay neurons (McCormick and Pape, 1990; McCormick and Huguenard, 1992; Huguenard and McCormick, 1992; Williams et al., 1997).

Subthreshold oscillations are present in the brain at various locations. We will focus on the oscillations that depend on the activation of a persistent type of sodium current, and not on the oscillations that depend on calcium conductance (Llinas and Yarom, 1986; McCormick and Huguenard, 1992). Even models that use a persistent sodium conductance often focus on an interplay with a slow potassium conductance, as in models of subthreshold oscillations in somatosensory cortex (Wang, 1993), frontal cortex (Gutfreund et al., 1995), and amygdala (Pape et al., 1998). In contrast to these models, subthreshold oscillations can also be obtained due to an interaction of the persistent sodium current with the hyperpolarization activated current (Alonso and Llinas, 1989). This interaction has previously been proposed as the basis for subthreshold membrane potential resonance in response to oscillatory intracellular current injection in the sensorimotor cortex (Hutcheon et al., 1996a,b). Previous simulations of entorhinal cortex SCs have incorporated a representation of persistent Na current and a slow outward current (K) or deactivation of a slow inward current (h), in order to perform a bifurcation analysis (White et al., 1995) and to study the role of channel noise (White et al., 1998). More recently, these simulations have been undertaken in order to analyze resonance properties (Brunel et al., 2001; Erchova et al., 2001) and synchronization properties (Acker et al., 2001). In the present study, we have analyzed the generation of subthreshold oscillations by combining data and modeling work on the slowly inactivating “persistent type” Na current (Alonso and Magistretti, 1998; Magistretti and Alonso, 1999; Magistretti et al., 1999a,b), and new data on the hyperpolarization activated h-current (Dickson et al., 2000), both in SCs of the entorhinal cortex. In Dickson et al. (2000), we used a one-compartment model to study the interaction of I_{NaP} and I_h qualitatively. The present work first presents an analysis of the validity of using a Hodgkin-Huxley type gate model for I_h , and provides a more accurate formulation of the kinetics in the voltage interval of the subthreshold oscillations. We also analyze the contribution of the deactivation of I_h at more

depolarized potential levels during spiking. For I_{NaP} , the slow inactivation is included to provide a more complete model. We also make more detailed comparisons to voltage-clamp and current-clamp data of, e.g., membrane potential sag and oscillations. Moreover, the role of I_h in, e.g., action potential shape, mAHP, and spike clustering, is also studied. In the second part of this report, we show that the I_h and I_{NaP} models still produce oscillations in the presence of other currents with their respective kinetics. For I_h , we analyze the two components, the fast and the slow, separately and study their respective roles in oscillations and action potential clustering. For clustering, the analysis is extended to include $I_{K(AHP)}$, and we show support for the involvement of both $I_{K(AHP)}$ and I_h in clustering. Finally, the use of a multi-compartment model permitted the study of the effects of a nonuniform conductance distribution, as well as possible components of space clamp in the experimental data. The initial results of the present work have been reported in abstract form (Fransén et al., 1998).

MATERIALS AND METHODS

Biophysical Simulation

Biophysical simulations were developed using the GENESIS simulation package (Bower and Beeman, 1995). These simulations focus on the reproduction of both voltage-clamp and current-clamp experimental observations to analyze whether the interaction of I_h and the persistent sodium current could underlie the subthreshold MPOs observed in these neurons. Simulation of the voltage-clamp data on I_h presented in Dickson et al. (2000) was combined with simulations of the voltage-clamp data on the persistent-type sodium current published separately (Magistretti and Alonso, 1999; Magistretti et al., 1999a,b).

In these simulations, the entorhinal cortex layer II SC (Klink and Alonso, 1997c) has been reduced to an equivalent cylinder model composed of seven compartments (Fig. 1C). One compartment represents the soma; one compartment represents the initial segment; three compartments connected in succession represent the primary, secondary, and tertiary segments of a single principal dendrite (to provide appropriate dendritic attenuation for synaptic inputs to the cell); and two connected compartments represent all remaining dendrites lumped together to constitute the main “load” to the soma. The proximal of the principal compartments and the proximal of the lump compartments and the initial segment are all connected to the soma. The lengths and cross sections of the three principal dendrite compartments were adjusted to give the dendrite a length constant of 2 (sealed-end condition). The compartment profile is found in Table 1. Further, resting membrane potential, input resistance, and membrane time constant were adjusted to comply with this experimental data.

Passive parameters

$$\begin{aligned} R_M &= 5.0 \Omega m^2 \quad (50,000 \Omega cm^2) \\ R_A &= 1.0 \Omega m \quad (100 \Omega cm) \\ C_M &= 0.01 F/m^2 \quad (1.0 \mu F/cm^2) \\ E_m &= -0.083 V \quad (83 mV) \end{aligned}$$

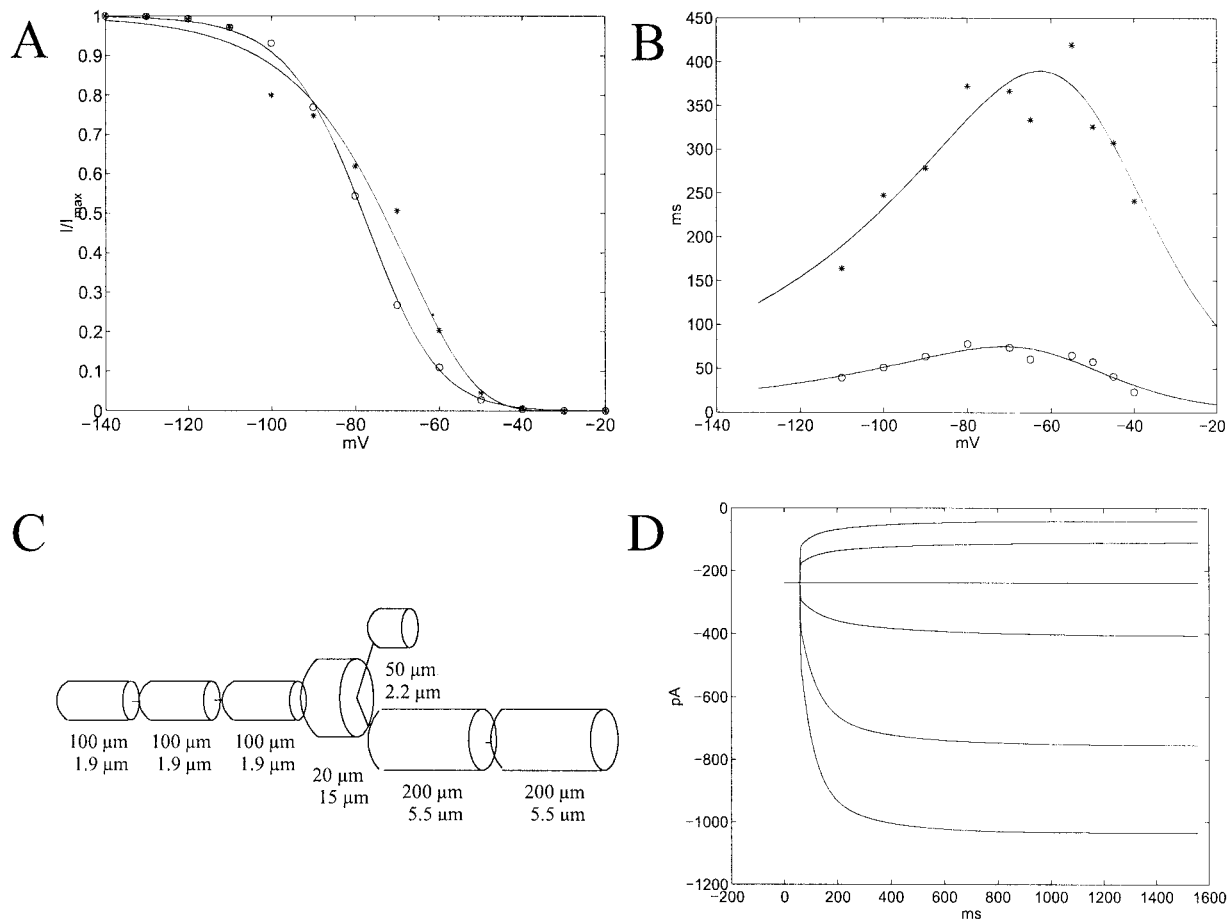


FIGURE 1. Model of voltage-clamp data on the hyperpolarization activated cation current (I_h). **A:** Model of steady-state activation of I_h found in normalized tail current data from voltage-clamp experiments. The fast component, which is the steeper one, has data points indicated by circles. The slow component has data points indicated by asterisks (*). **B:** Time constants were derived from activation and deactivation data. As noted in the physiological results, two exponents had to be used to obtain the best fit to the activation and deactivation data, resulting in two separate time constants at each voltage level (fast time constants indicated by circles, slow time constants by asterisks). The voltage dependence of the time constants was described by two dual exponential equations of membrane potential (solid lines), with a fast component maximum at ~ 80 ms and the slower component maximum ~ 400 ms. **C:** Schematic representation of the compartment-

tal model used in the simulation of the intrinsic properties of stellate cells. The dimensions of each component of the model are summarized. **D:** Simulation of the multi-compartment model with minimal set of currents ($I_h + I_{NaP} + I_{K(leak)}$) showing time course of I_h currents derived from voltage-clamp data during a step change from -60 mV to -70 , -90 , -110 mV and to -50 , -40 mV in the activating and deactivating direction, respectively. Note the similarity of the time course of the current with physiological data shown in Figure 5A,B of Dickson et al. (2000). Absolute current levels were derived from the steady-state current at -90 mV, corresponding to approximately 50% activation. The data were obtained by subtraction of currents observed by total blockade of I_h (corresponding to the experimental application of ZD7288) from those observed in control conditions.

The value of the membrane reversal potential E_m depends on contributions from leakage Na^+ and leakage Cl^- currents (the K^+ leak current is represented explicitly as a separate current). One may also view synaptic background activation with slow kinetics, e.g., N-methyl-D-aspartate (NMDA) and γ -aminobutyric acid ($GABA_B$), as part of the leakage current. Note that as the K^+ current is represented separately, its conductance should be added to the value of R_M given above when comparing to other data.

Previous simulations have used a wide range of membrane currents to replicate sharp electrode current-clamp recordings from these neurons (Fransén et al., 1998, 1999). Those simulations included Hodgkin-Huxley currents underlying spike generation. The simulations presented in the latter portion of this report present a revision of this multi-current model with the newly de-

veloped models of I_h and I_{NaP} . However, in order to analyze fully the interaction of specific currents in generation of subthreshold oscillations, the simulations presented in the first part of the present report used a simplified neuronal representation containing only the hyperpolarization activated nonspecific cation current (I_h), the persistent low-threshold sodium current (I_{NaP}), and the potassium leak current ($I_{K(leak)}$). For the simplified model, we thus have

$$I_{ion} = I_h + I_{NaP} + I_{K(leak)}$$

The dynamics of these currents were represented using the formal structure of the Hodgkin-Huxley equations (Hodgkin and Huxley, 1952) with the parameters listed in the following equations (membrane potential V in volts, time in seconds):

TABLE 1.

Compartment Profile With Conductances for the Currents

Compartment	Length (μm)	Diameter (μm)	gH (fast) (S/m ²)	gH (slow) (S/m ²)	gNaP (S/m ²)	gK (leak) (S/m ²)
Soma	20	15	0.98	0.53	0.38	0.58
IS	50	2.2	0.0	0.0	0.0	0.58
Proximal dendr	100	1.9	0.98	0.53	0.38	0.58
Medial dendr	100	1.9	0.98	0.53	0.38	0.58
Distal dendr	100	1.9	0.98	0.53	0.38	0.58
Proximal lump	200	5.5	0.98	0.53	0.38	0.58
Distal lump	200	5.5	0.98	0.53	0.38	0.58

IS, initial segment compartment; dendr, principal dendrite compartment.

h-current

Reversal potential $E_{rev} = -0.020$ V

Activation:

$$\tau_m(\text{fast})(V) = \frac{0.00051}{\exp[(V - 0.0017)/0.010] + \exp[-(V + 0.34)/0.52]}$$

$$\tau_m(\text{slow})(V) = \frac{0.0056}{\exp[(V - 0.017)/0.014] + \exp[-(V + 0.26)/0.043]}$$

$$m_{\text{inf}}(\text{fast})(V) = \frac{1}{(1 + \exp[(V + 0.0742)/0.00978])^{1.36}}$$

$$m_{\text{inf}}(\text{slow})(V) = \frac{1}{(1 + \exp[(V + 0.00283)/0.0159])^{58.5}}$$

Gate exponent = 1

NaP current

Reversal potential $E_{rev} = +0.087$ V

Activation:

$$\alpha_m(V) = \frac{0.091 \cdot 10^6(V + 0.038)}{1 - \exp(-(V + 0.038)/0.005)}$$

$$\beta_m(V) = \frac{-0.062 \cdot 10^6(V + 0.038)}{1 - \exp((V + 0.038)/0.005)}$$

$$\tau_m(V) = \frac{1}{\alpha_m + \beta_m}$$

$$m_{\text{inf}}(V) = \frac{1}{1 + \exp[-(V + 0.0487)/0.0044]}$$

Gate exponent = 1

Inactivation:

$$\alpha_h(V) = \frac{-2.88V - 0.0491}{1 - \exp[(V - 0.0491)/0.00463]}$$

$$\beta_h(V) = \frac{6.94V + 0.447}{1 - \exp[-(V + 0.447)/0.00263]}$$

$$\tau_h(V) = \frac{1}{\alpha_h + \beta_h}$$

$$h_{\text{inf}}(V) = \frac{1}{1 + \exp[(V + 0.0488)/0.00998]}$$

Gate exponent = 1

The “persistent-type” slowly inactivating Na⁺ current was modeled according to Magistretti and Alonso (1999) and Magistretti et al. (1999a,b) for the steady-state activation and inactivation and kinetics of inactivation, and for the reversal potential. It was modeled according to McCormick and Huguenard (1992) for the kinetics of activation and the exponents of the activation rates m, h. The maximal conductance was adjusted to the conductance of I_h to permit the development of subthreshold oscillations.

The K(leak) conductance was considered to be linear and uniformly distributed with a conductance of 0.58 S/m² (58 μS/cm²) and a reversal potential E_{rev} = -0.083 V. The value of the reversal potential was taken from Dickson et al. (2000).

The resulting passive properties of the simulated neuron were as follows:

Resting membrane potential -53.5 mV

Input resistance 130 MΩ (this reduced to 50 MΩ after the “sag” caused by activation of I_h) for a hyperpolarizing current step

Membrane time constant 10 ms

Length constant of dendrite 2

The method for numerical solution to differential equations was the default exponential Euler method. A time step of 50 μs was used for the current-clamp simulations and a time step of 5 μs for the voltage-clamp simulations. For the analysis of experimental voltage-clamp data, Origin 4.1 was used. For the curve fitting, the simplex algorithm in the optimization tool box in Matlab 5.2 was used.

The current-clamp simulations included a conductance-based noise source. This represents potential effects of channel noise (White et al., 1998; Shalinsky et al., 2002) or synaptic noise in actual neural function. The noise was generated from a Poisson process with a mean of 200 Hz, reversal potential 45 mV, time constant 3 ms, and conductance 9.4 pS, and was placed on the proximal lumped dendritic compartment. It may

TABLE 2.

Compartment Profile of the Full Model[†]

Current	IS (S/m ²)	Soma (S/m ²)	Prox + med dendr/lump (S/m ²)	Dist dendr/lump (S/m ²)
gNa	150	38	38	19
gK _{dr}	215	107	107	54
gK _C	0.0	13,400	0.0	0.0
gK _{AHP}	0.0	0.1	0.1	0.1
gCa _L	0.0	1.0	1.0	1.0
gCAN	0.0	280.0	0.0	0.0
gH (fast)	0.0	1.12	1.12	1.12
gH (slow)	0.0	0.605	0.605	0.605
gNaP	0.0	0.69	0.69	0.69
gK (leak)	1.2	1.2	1.2	1.2
ϕ _{Ca(K_{AHP})pool}	0.0	61.34 · 10 ¹²	97.37 · 10 ¹² /16.73 · 10 ¹²	21.91 · 10 ¹² /3.76 · 10 ¹²

Prox, proximal compartment; med, medial compartment; dist, distal compartment; dendr, principal dendritic compartment.

[†]Maximal conductances *g* and calcium conversion factor ϕ for each compartment. For some currents, the density was assumed to be uniform. For the others, the general profile, with a higher conductance at the soma, and gradually lower conductances for more distal dendritic compartments, was adopted from Traub et al. (1991). The criteria selected to adjust the conductances do not give a unique solution (Traub et al. 1991; DeSchutter and Bower, 1994).

be noted that the occurrence and stability of MPOs did not require the presence of noise (data not shown), but its presence increased the parameter interval within which oscillations were stable (see Discussion).

To verify that the oscillations produced by I_h and I_{NaP} are intact when all the major currents are present, as well as to study the spike clustering of the SCs, we developed a model with a wider range of additional membrane currents, including the Na^+ and K^+ currents responsible for fast action potentials, a high-threshold Ca^{2+} current, a calcium-dependent K^+ current, a fast calcium- and voltage-dependent K^+ current, and a nonspecific Ca^{2+} -dependent cationic current. See Appendix 1 for the details of these currents and Table 2 for the respective conductances used.

RESULTS

Biophysical simulation of the detailed data on the activation kinetics of I_h provided further evidence for its potential interaction with the persistent sodium current in generating subthreshold MPOs and spike clustering. Therefore, the h-channel model was first analyzed before we addressed how specific aspects of the h-current could be involved in oscillations and spike clustering. The SC model was first used to fit the voltage-clamp data on I_h , and was then combined in the simulation with the persistent sodium current (Magistretti and Alonso, 1999; Magistretti et al., 1999a,b) to simulate the current-clamp data.

h-Channel Gate Model

The I_h current was modeled with equations in the Hodgkin-Huxley formalism, as described in the Materials and Methods section. It

showed a linear (ohmic) instantaneous I - V relation and had a limiting relaxation (a slope smoothly approaching zero in both ends) up and down for the steady-state activation. Time constants were derived from activation and deactivation data. In the fit to find the time constant for each voltage level for activation and deactivation, two exponents had to be used, indicating biphasic kinetics. The voltage dependence of the time constant was described by two bell-shaped functions of membrane potential, the faster component with a maximum of ~ 80 ms and the slower component a maximum of ~ 400 ms (Fig. 1B). For the curve fitting, the common biexponential curve was used. The relative contribution from each component to the conductance varied with voltage, and to vary the conductances accordingly, two steady-state activation curves were used, as discussed below. The steady-state activation of I_h was in the first step described by a Boltzmann-style equation. The steady-state activation curve was fitted to normalized tail current data. The experimental data showed no sign of inactivation. A weighted higher-order Boltzmann curve (with the exponent as a free parameter in the optimization) was used in the next step to get a good fit of the data in the most depolarized region. This turns out to be important, as this is the region in which the oscillations develop; a fit with an exponent of 1 causes a large overestimate of the current, and underestimates the derivative of the current. Using the amplitude of the two time constants of activation (the coefficients of the exponential fitting functions), steady-state activation curves were derived for each of the two components (Fig. 1A). Thus, in effect the two components, fast and slow, were independently modeled with equations in the Hodgkin-Huxley formalism, which is summarized below.

A reversal potential of -20 mV, derived from experimental data (Dickson et al., 2000), was used. In the experiments, the reversal potential from chord conductances was compared to I - V extrapolation. A gate exponent of 1 was determined from the time course

of activation in voltage-clamp data. The activation state variables, m_{fast} and m_{slow} , thus had gate exponents of 1, but the steady-state activation $m_{\text{inf}}(\text{fast/slow})$ had exponents of 1.36 and 58.5, respectively. Different exponents are necessary when the steady-state activation curve needs a higher rate for a good fit, but the time course of activation does not show much delay (Huguenard and McCormick, 1992). The maximal conductance of I_h , G , was adjusted to give a current of the order measured in whole cell patch clamp recordings at -60 mV. The initial conductance of the I_{NaP} was similarly adjusted, and fine-tuning was done by studying the generation of MPOs.

In summary:

$$I_b = I_b(\text{fast}) + I_b(\text{slow}) = G(m_{\text{fast}} + m_{\text{slow}})(E - E_{\text{rev}})$$

and the fast and slow state variables m_{fast} and m_{slow} obey

$$\frac{dm}{dt} = \alpha_m(1 - m) - \beta_m m \quad \text{where}$$

$$\alpha_m = \frac{m_{\text{inf}}}{\tau_m} \quad \text{and} \quad \beta_m = \frac{(1 - m_{\text{inf}})}{\tau_m}$$

Voltage-Clamp Simulations

The model of I_h was evaluated in a voltage-clamp simulation. Whereas the one-compartment model used in Dickson et al. (2000) was able to reproduce the general features of the current response, we were able to show in this work that the use of a multi-compartment model further increased the fit to data. Using the derived equations for I_h , voltage-clamp simulations were thus performed with the multi-compartment model described in the Materials and Methods. The result was compared to the experimental data, as shown in Figure 1D. The simulated voltage-clamp currents show good agreement with experimental data in time course and relative amplitude. The simulation also effectively represents the change in voltage-clamp properties induced by ZD7288 (see Fig. 5 in Dickson et al., 2000). The contribution of the multi-compartment model was most notable in the time period following a step in voltage (see also the discussion on space clamp). With the multi-compartment model, we were also able to study the effects of a nonuniform distribution of channel conductances. With a high distal and low proximal and medial conductance of I_h , the fit to voltage-clamp data improved further (data not shown, see also the Discussion).

Membrane Potential Sag and Oscillations

The model was used to simulate current-clamp phenomena, including the ‘‘sag’’ in membrane potential during hyperpolarizing current steps and the subthreshold MPOs. The simulation of the sag in membrane potential is shown in Figure 2A and the simulation of subthreshold MPOs in Figure 2B–D.

Generation of subthreshold MPOs required combining the I_h current with a representation of the persistent low-threshold sodium current. The simulations show that an interplay between I_h and I_{NaP} is necessary to account for the generation of MPOs in layer II SCs, as shown in Figure 2C. Figure 2C also shows the relative time course of the increase in persistent sodium during the

depolarizing phase of oscillations, followed by the increase in I_h during the hyperpolarizing phase of oscillations. The oscillations depend on the delayed feedback from I_h . Interestingly, if the time constants for activation of I_h were set to be the same as the time constants for I_{NaP} , there were no oscillations (data not shown).

For the minimal model containing only I_h , I_{NaP} , and $I_{\text{K(leak)}}$, the stimulation current used to test oscillations at different levels was negative as many currents influencing membrane potential are missing. In the more complete model, this is no longer the case and stimulation intensities are positive.

Simulation of the partial blockade (65%) of I_h by cesium caused a decrease in the amplitude and frequency of subthreshold oscillations corresponding to that observed in current-clamp recordings (Fig. 3A). In the experiments, the blockade was estimated to be 60–75% in 2 mM Cs. The oscillations became unstable, with either dampened or growing amplitudes, around a block of 72%, indicating the approximate blocking needed to prevent stable oscillations. In consequence, and as observed experimentally with ZD7288, full block of I_h in the model also completely abolished the oscillations (data not shown). Simulation of the blockade of the leak current by barium (paired with blockade of synaptic ionotropic transmission) caused an increase in amplitude of oscillations accompanied by a small slowing of frequency (Fig. 3B), as in experiments (Dickson et al., 2000).

Figure 4A presents a phase diagram plotting I_h current against the I_{NaP} current, illustrating the cyclical interaction of these currents, which underlies the subthreshold MPOs in the simulation. The power spectrum of the subthreshold oscillation data is shown in Figure 4B, illustrating the peak at 3.0 Hz.

The current of I_h and I_{NaP} for a linear current ramp is shown in Figure 5A. It is shown that the amplitude of the membrane oscillation follows an inverted U-shape relative to injected current (Fig. 5B), as in experiments (Alonso and Klink, 1993) (Fig. 4C). The amplitude of oscillations initially increases and then decreases as current injection increases. This occurs because over the interval, I_{NaP} increases (Fig. 55D) and I_h decreases (Fig. 55C), giving a window of sufficient combined current for the oscillations. Thus, I_{NaP} limits the amplitude as the injected current decreases and I_h limits the amplitude as the injected current increases.

To study the relative importance of the fast and slow component of I_h for the oscillations, the two components were studied separately for two consecutive periods of oscillations (Fig. 6A). As can be seen, the fast component shows a relative larger variation in conductance, the slow component remaining almost constant. In terms of current, the difference between maximum and minimum activation is 17-fold larger for the fast than for the slow component. In a separate test, the fast component was given a very slow time constant of 10 s. No oscillations were observed within the full range from resting to tonic firing (data not shown). We conclude that the fast component is the major factor in the oscillation generation.

Medium AHP and Clustering

In experimental data, the action potential of the SCs is followed by a stereotyped mAHP (Alonso and Klink, 1993). Given the fast kinetics of I_h in the SCs, it is possible that I_h also contributes and/or is a major determinant of the mAHP in these neurons. In fact,

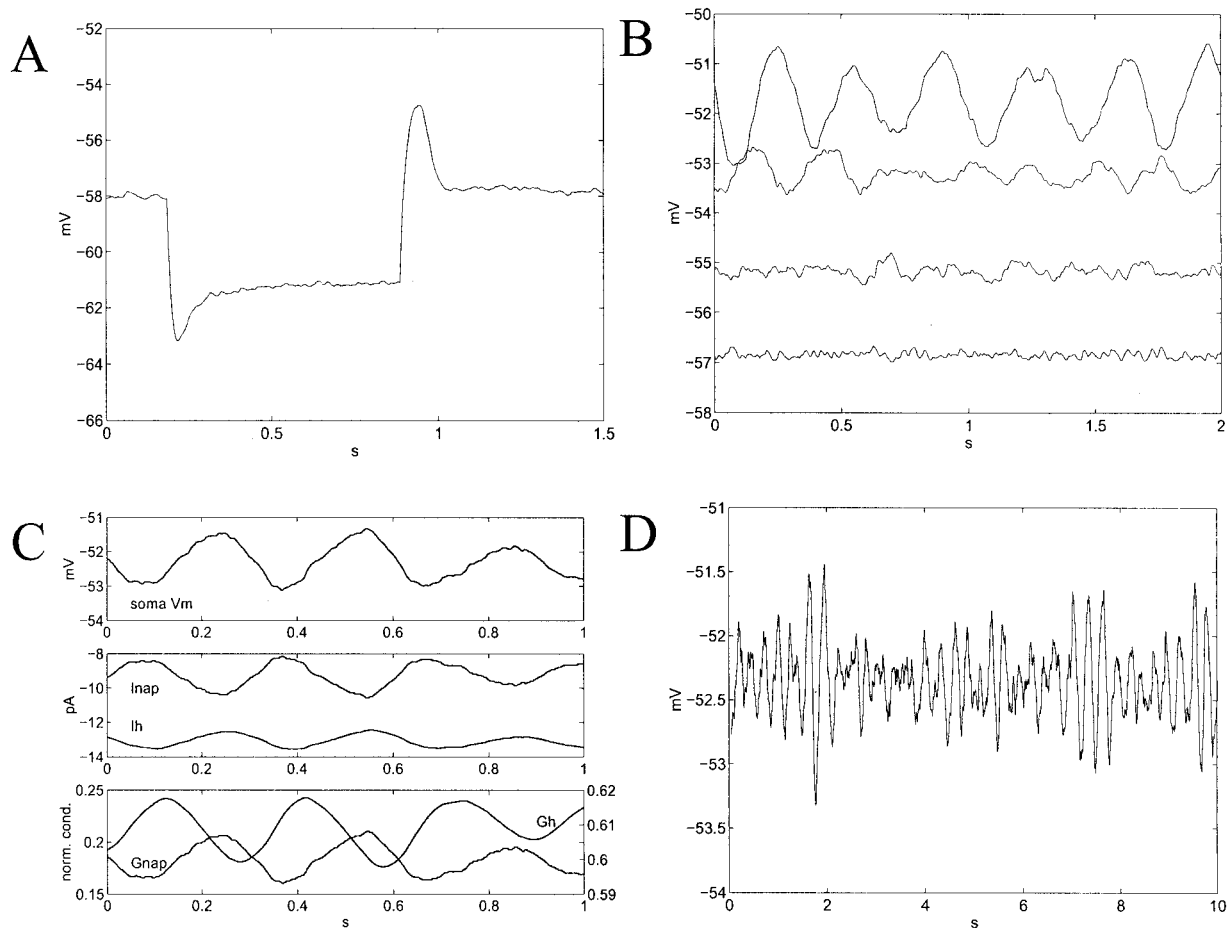


FIGURE 2. Minimal model sag and oscillations. **A:** Simulated membrane potential trace demonstrating the “sag” in membrane potential due to activation of I_h during a hyperpolarizing current step of -0.05 nA. Note the similarity of the time course of sag with physiological data shown in Dickson et al. (2000); see Fig. 2A. (The absence of voltage-dependent sodium and delayed rectifier currents in the simplified simulation results in a depolarizing overshoot without action potentials at the end of current injection.) The sag% is 38%, within the experimentally reported value of 30% for sharp electrodes (Alonso and Klink, 1993) and of 48% for whole cell patch recording (Dickson et al., 2000). **B:** Simulation of subthreshold membrane potential oscillations arising from interaction of I_h and I_{NaP} . At depolarized values, the membrane potential undergoes oscillations of a frequency and amplitude corresponding to those observed in experiments (Dickson et al., 2000; see Fig. 1D). **C:** Changes in I_h and I_{NaP}

during subthreshold oscillations. Note that increases in I_h due to hyperpolarization correlate with the onset of the rising phase of oscillations, after which increases in I_{NaP} provide the driving force for depolarization. Decreases in I_h due to depolarization correlate with the peak of membrane potential and onset of the falling phase of the oscillation. (I_h and I_{NaP} are the only voltage-dependent conductances in this simulation). To see the two components of I_h separately during an oscillation, see Fig. 6A. Bottom left scale I_{NaP} , right scale I_h . The phase shift between I_h and I_{NaP} is 213 degrees lagging I_{NaP} (+33 degrees from out of phase, as compared to the experimental value of +40 in Dickson et al., 2000). As in experiments (Alonso and Klink 1993; Fig. 4A), the oscillations are frequently asymmetric, with the rising phase showing a smaller slope than the falling phase. See the discussion for further details. **D:** Simulation of sustained subthreshold oscillations. Oscillation frequency is 3.3 Hz.

block of I_h with ZD7288 largely reduces the mAHP (Dickson et al., 2000) which, in contrast, is minimally affected by Ca-conductance block (Alonso and Llinas, 1989; Klink and Alonso, 1993). Figure 6B demonstrates that a rapid depolarization by a current pulse mimicking an action potential causes a fast and substantial deactivation of the I_h current. Thereafter, during the hyperpolarization, I_h activates progressively, while I_{NaP} remains relatively constant. The net effect, compounded with the membrane time constant, produces a time course of repolarization analogous to the medium afterhyperpolarization observed in current-clamp recordings. The U shape of the membrane potential constituting the mAHP can be understood by studying the sum of I_h and I_{NaP} . After the action potential and fAHP, there is a net outward current,

due to the leakage current, which gradually hyperpolarizes the cell. As I_h activates, the outward current decreases, and at the bottom of the mAHP, the sum of I_h and I_{NaP} balances the leakage current. The continued activation of I_h eventually brings the membrane back to resting.

Stellate cells typically fire in clusters. To study the spike clustering of the SCs, we developed a model with a wider range of additional membrane currents, including the Na^+ and K^+ currents responsible for fast action potentials, a high-threshold Ca^{2+} current, a calcium-dependent K^+ current, a fast calcium- and voltage-dependent K^+ current, and a nonspecific Ca^{2+} -dependent cationic current. For the more complete model, we thus have

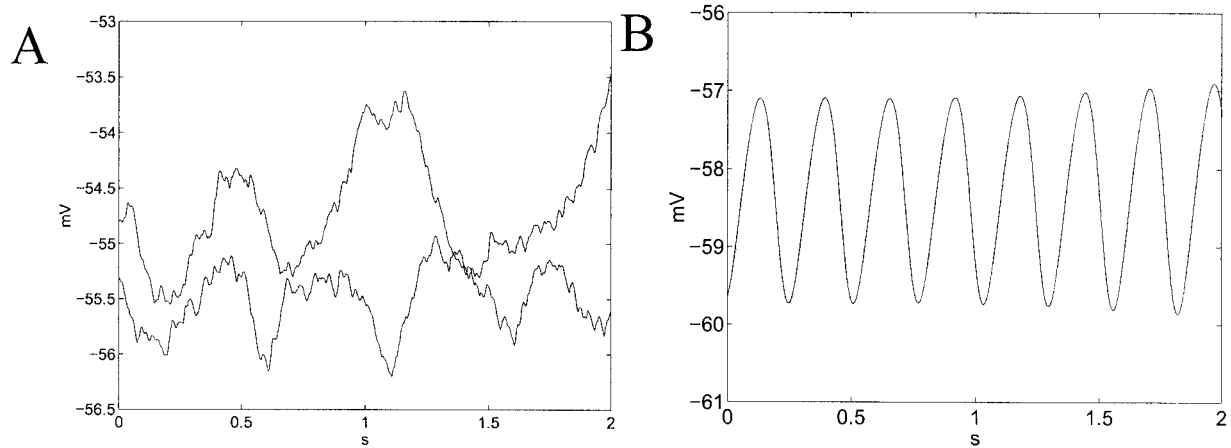


FIGURE 3. Minimal model blockade simulations. A. Simulation of the effects of cesium by reducing I_h conductance by 65% (lower trace) causes a decrease in amplitude (to ~ 1 mV) and frequency (to ~ 2 Hz) of oscillations, which become more irregular. Simulations with a blockade of 72% become unstable (upper trace). **B:** Simulation of the effects of barium by blockade of the $K(\text{leak})$ current by 100%

(synaptic transmission, e.g., synaptic noise is also blocked by 100% because the experiments were conducted with excitatory and inhibitory synaptic transmission blockade). Membrane potential oscillations increase in amplitude and show a slight decrease in frequency (i.e., 3.7 Hz) (consistent with Dickson et al., 2000; see Fig. 10F).

$$I_{\text{ion}} = I_{\text{Na}^+} + I_{\text{K}_{\text{dr}}} + I_{\text{CaL}} + I_{\text{K}_{\text{AHP}}} + I_{\text{K}_{\text{C}}} + I_{\text{CAN}} + I_b + I_{\text{NaP}} + I_{\text{K}(\text{leak})}$$

See Appendix 1 for details on these currents. This model enables a comparison to spiking data from experiments conducted with sharp electrodes (Alonso and Klink, 1993; Klink and Alonso, 1993). The more complete model is compared to data conducted at 35°C. To compensate for this increase of 11°C, we used shorter current time constants and higher current conductances. We used a Q10 of 4.5 (Magee, 1998) for the h-activation time constant. The higher conductances used give a smaller input resistance and a shorter membrane time constant, in accord with experimental data.

Figure 7A,B displays the transition in the model from oscillations via single spiking to clustering and finally tonic firing. The

cluster frequency of the middle trace is 1.3 Hz. The experimental data for the cluster frequency have a range of 1–3 Hz (commonly ~ 1.6 Hz). The frequency within clusters is ~ 4 Hz, which is lower than in experiments, where within cluster frequencies are ~ 10 Hz. The calcium-dependent potassium current K_{AHP} is a possible main contributor to clustering. In accord with experimental data (Klink and Alonso, 1993) (Fig. 2), blockade of calcium influx in the model caused a significant reduction in clustering, resulting in a more direct transition from subthreshold oscillations and single spikes to tonic firing when the stimulating current is increased (data not shown). Changes in the conductance of the Ca-sensitive K-current K_{AHP} were analyzed in detail, as shown in Figures 8B and 9B,C, as discussed below.

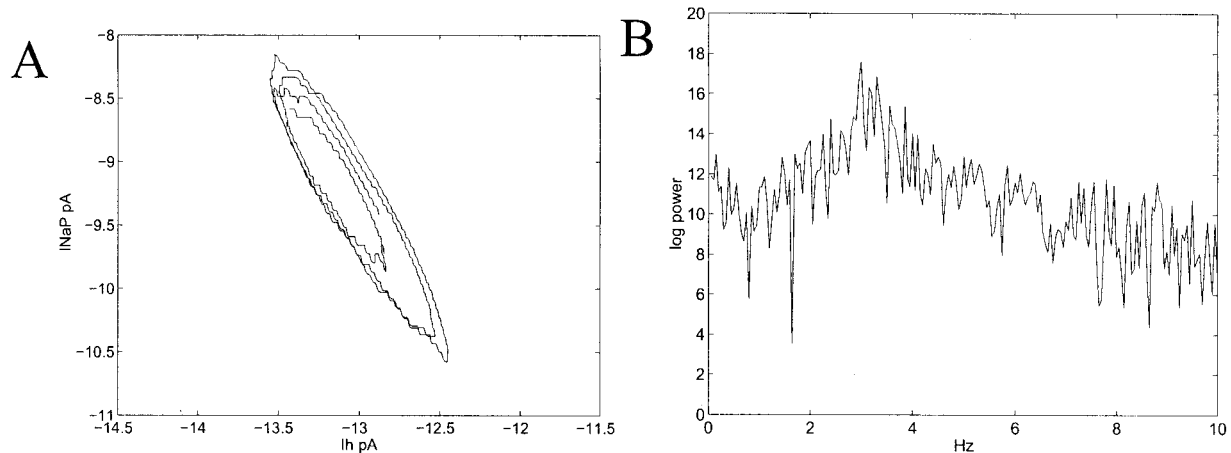


FIGURE 4. Minimal model phase plane and frequency analysis. A: Simulation data showing a phase plane plot of NaP current versus h-current during the subthreshold membrane potential oscillations shown in Fig. 2C. These currents trace an elliptical circuit through current space during their oscillatory interaction. **B:** Power spectrum

of simulation data during subthreshold membrane potential oscillations showing peak in the power spectrum at ~ 3.0 Hz, within the range of the experimental data 3.1 ± 0.7 Hz. Twenty seconds of data was used for the analysis.

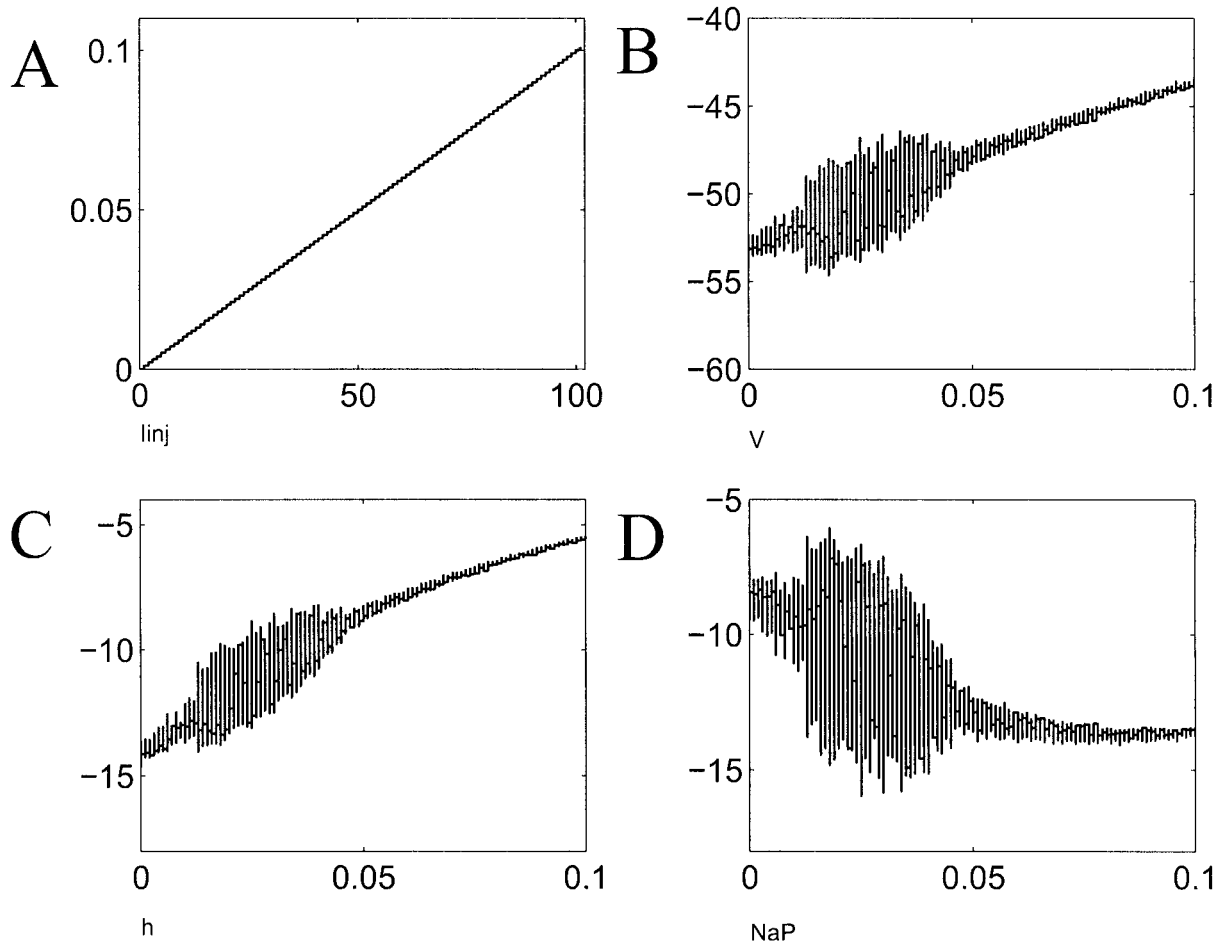


FIGURE 5. Minimal model showing the development of oscillations during a current ramp. **A:** Simulation consisted of a 100-s linear ramp of the current from 0 to 0.1 nA. **B:** Soma membrane potential. The amplitude of the membrane potential oscillation is shown to follow an inverted U-shape, as in experiments (Alonso and Klink 1993; Fig. 4C). That is, increases in current injection initially cause increased amplitude of oscillations but eventually lead to a decrease in oscillations amplitude. The average frequency of oscillations was 2.8

Hz. **C,D:** Over the interval of injected current values between 0 and 0.1 nA, the I_{NaP} increases (C) and I_h decreases (D), giving a window of sufficient combined current for the oscillations. Thus, the decreasing NaP current limits the amplitude as current injection decreases, and the h -current limits the amplitude as the current injection increases. Ionic currents (pA) are plotted on the y-axis relative to injected current (nA) plotted on the x-axis.

The subthreshold oscillations persist in this larger model. Figure 7A demonstrates the appearance of subthreshold MPOs in the more detailed simulation. The additional currents thus do not prevent the appearance of subthreshold MPOs. Figure 7A presents traces of increased current injection showing initiation of subthreshold oscillations, increased amplitudes, and single spiking. The frequency of the oscillation is ~ 9 Hz for the top trace and 12 Hz for the two traces below this. The experimental range is 5–12 Hz, with an average of 8.6 Hz. The amplitude of the oscillations ranges within 0.2–1.7 mV. The experimental range is 0.5–9.7 mV, with an average of 2.6 mV. The oscillations develop slightly above -60 mV and the first spikes appear for an average potential around -54.5 mV; both values are in accord with experimental data. The AHP only goes to potentials around -62 mV, also in accord with experimental data.

The model also now shows the rebound spiking of SCs. If the cell is released from a hyperpolarized potential of sufficient depth, the cell fires a rebound action potential (Fig. 7C). The sag shown

led to a percentage change (sag%) relative to baseline of 28, as compared to the experimental value for sharp electrodes of 30% (Alonso and Klink, 1993). The dash-dotted line in Figure 7 also depicts a cell with all the h -current placed on the fast component; the dashed line represents all current on the slow component. With the fast component, a rebound produces a spike followed by a hyperpolarization. With only the slow component, two spikes are produced, followed by an increased depolarization, indicating a potential role of the slow component in clustering.

To study further the role of the currents I_h , I_{NaP} , and $I_{K(AHP)}$ in the clustering, these currents were plotted in a three-dimensional (3D)-phase plane (Fig. 8). A linear current ramp injected in the soma produced the membrane potential record shown in Figure 8A. As would be expected, and in accordance with experiments, oscillations develop first, followed by single spikes, clustering, and finally tonic firing. Single spikes separated by one or two cycles of subthreshold oscillations are present, as well as cluster doublets and multiplets. A spike may thus be preceded by either a spike, one

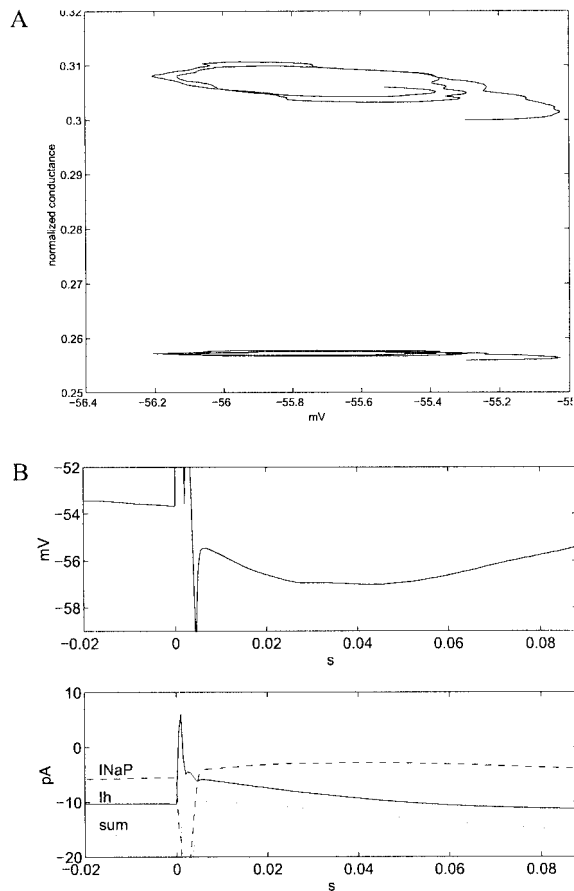


FIGURE 6. Minimal model, showing analysis of generation of oscillations and of mAHP. **A:** The fast component of I_h is responsible for subthreshold oscillations. A linear current ramp simulation is carried out. Two consecutive cycles of oscillations are used. The fast (upper trace) and slow component's normalized conductances (lower trace) are plotted versus membrane potential (around -55 mV). As shown, the slow component is almost constant. The fast component gives 17 times larger variation in current than the slow component, i.e., it is the major factor in the oscillation. **B:** Simulation demonstrating potential role of I_h in medium afterhyperpolarization (mAHP). **Top:** Membrane potential trace showing the fAHP and mAHP appearing directly after an action potential-like current stimulation. **Bottom:** Changes in I_h and I_{NaP} current during the mAHP, showing a strong decrease in I_h induced by the brief depolarization of the action potential, with a time course corresponding to that of the mAHP. To see how I_h conductance develops during a spike, see Fig. 9A,C,D. I_h , I_h current; I_{NaP} , I_{NaP} current; sum, sum of I_h and I_{NaP} .

oscillation, or two oscillations. In the phase plane plot of the currents (Fig. 8B), it can be seen that there are three different families of trajectories for a spike, depending on whether it is preceded by two (A), one (B), or no (C) oscillations. Thus, the history of the potential in terms of oscillations and spikes can be extracted by observing the family (A, B, or C) within which a curve falls. The main difference separating the families is along the vertical $I_{K(AHP)}$ -axis, indicating that this is the main contributor to this segregation. This shift can also be seen in Figure 9C for the conductance of $I_{K(AHP)}$ for two consecutive spikes in a cluster.

$I_{K(AHP)}$ is not, however, the only factor influencing the clustering. Based on experimental observations that the block of I_h by

ZD7288 was commonly accompanied by an increased spike width and decreased fast AHP (Dickson and Alonso (unpublished data)), we were interested in studying whether I_h also had a role in the clustering. Results from simulations supported this, as was already discussed in relation to Figure 7C. The fast and slow components were studied separately. As can be seen in Figure 1B, the fast component has a very fast time constant during a spike, i.e., it closes completely at an early point. As can be seen, there are only data up to -40 mV. This primarily affects the uncertainty of the slow component, as the fast component is already relatively close to its closed state. The slow component may also smoothly approach its closed state, or it may level off and reach a constant value above zero. The test described below was intended to investigate the sensitivity of the model to this uncertainty in the data, as well as to look in greater detail at the role of the slow component. In the model, the slow component has a minimum of 20% conductance during a spike, i.e., it never closes completely, in agreement with experimental data (Spain et al., 1987) and the data just outlined above. Our modeling gives three indications of the involvement of the slow component of I_h .

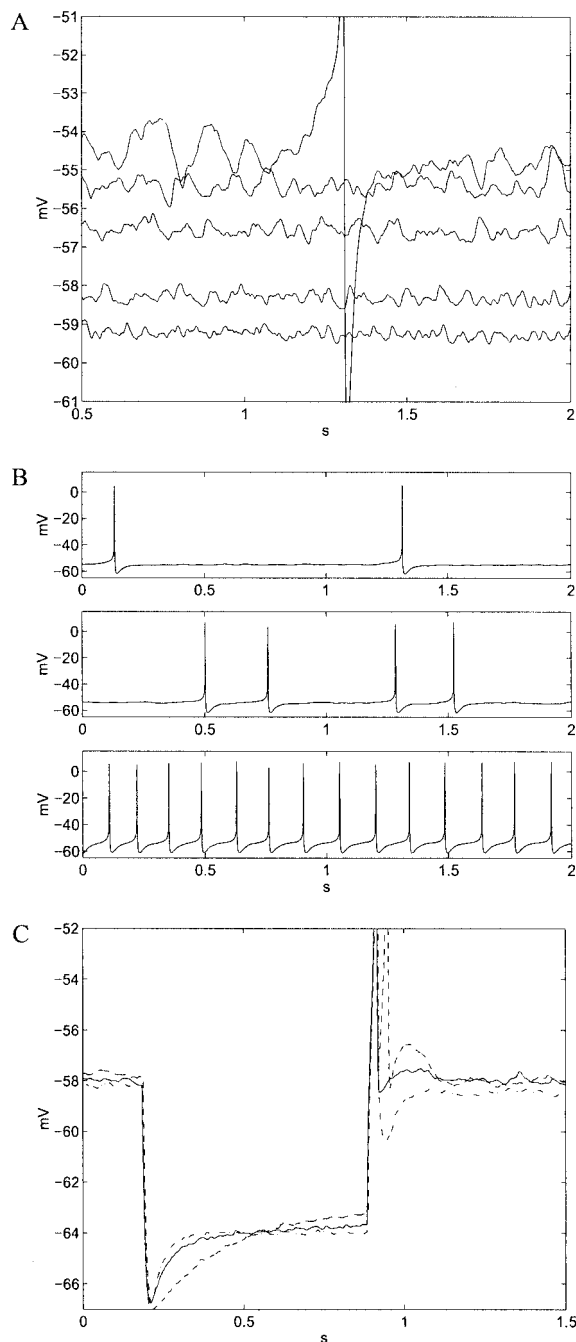
First, if the slow component is given a time constant of 10 s, only oscillations, single spikes and tonic firing is seen, but no clusters are seen within the full voltage interval from resting to tonic firing (data not shown).

Second, in Figure 9D (together with Fig. 9A,C), we demonstrate that the slow component shows a decrease in current over a period of two consecutive spikes in a cluster, whereas the fast component does not change. The conductance of $I_{K(AHP)}$ also shows a corresponding shift (data not shown). The reduction of the slow component during the second spike might be contributing to stopping the spiking, i.e., producing a cluster according to the following: During a spike, the h-current is deactivated, but it is then strongly activated during the following afterhyperpolarization (Fig. 9C as well as Fig. 6B). This induces a rebound current, similar to that seen after an experimentally induced hyperpolarization, that leads to a greater propensity for another spike to be generated after one has been generated (Fig. 7C). But, with reduced h-current, the rebound is also reduced. This may terminate spiking, forming a spike cluster out of what would otherwise have been tonic firing. The $K(AHP)$ current, which by itself can not produce clustering but only spike frequency adaptation, can however add to the termination of the cluster and hence play a role in the formation of clusters. More specifically, as noted above in relation to Figure 9D, the I_h reduction occurs primarily in the slow component. This component is relatively fast at depolarized levels during the spike (Fig. 1B), and thus has time to deactivate, but during the AHP and depolarization to threshold, the component attains its slowest kinetics and therefore does not have time to activate before the second spike appears.

Third, Figure 9B shows that both the time constant of the slow component, as well as the conductance of the $K(AHP)$ current, have a reasonably wide, but limited, interval that permits the occurrence of clusters. Figure 9 investigates the role of the slow component, together with the role of the $K(AHP)$ current. A set of simulations with a variation in conductance of $I_{K(AHP)}$ and a variation in time constant of the slow component was conducted. Every point shown in Figure 9 corresponds to a full run of a sweep

of the current from low to high. A dark square indicates a low rating of clustering and a bright square indicates a higher rating of clustering capability. From this simulation result, we draw the following conclusions. First, the clustering is a relatively robust phenomena, the regime of full function (white) is quite extended. Second, the two factors can be seen to limit the parameter region where clustering exists. The two factors set boundaries (black and dark gray), outside of which clustering does not occur but within which clustering of various forms can be sustained. For low values of $I_{K(AHP)}$ there is only tonic firing, for high values only single spikes and tonic firing. For small time constants of the slow I_h during the spike, (large value), there are only single spikes and tonic firing, for large time constants (low values) there is rarely good

clustering. Third, because of the presence of noise, the boundaries between firing modes (doublets, triplets, and mixed doublets/triplets) are not sharp. This was verified in a map winding number plot (a plot of the ratio between number of spikes and number of oscillations versus injected current), where no clear boundaries between the different firing modes were present, indicating that the system does not show mode locking (data not shown). Based on these observations, we may hypothesize that the I_h slow component time constant does not fall to very low values (in the range of ms), as the fast component does. As was demonstrated, when the time constant of the slow component becomes close in scale to the order of the spike duration (1 ms), the current closes almost completely, and apparently clustering is thereby prohibited. Thus, analysis of clustering indicates a possible role for both the $I_{K(AHP)}$ and slow component of the I_h current.



DISCUSSION

The simulation data demonstrate that representations of I_h and I_{NaP} based on voltage-clamp data (Fig. 1) interact in a manner which causes voltage “sag” and subthreshold oscillations resembling those observed during current-clamp recording (Fig. 2). This further supports the potential role of I_h in generation of subthreshold oscillations. In a model with a more complete set of currents, spike clustering is reproduced. The full model can show the full transition from subthreshold oscillations, through single spiking to spike clustering and tonic firing at higher intensities. In the simulation, the I_h and $I_{K(AHP)}$ currents are necessary for the appearance of spike clustering. Further, the possible role of I_h in the generation of the mAHP is studied. In the voltage interval -40 mV -10 mV, where no data are available, the model predicts that the slow component of I_h does not follow the fast component down to very short time constants. The model also predicts that the fast component of I_h is responsible for the involvement in generation of subthreshold oscillations, and the slow component dominates in the generation of spike clusters. Simulation of these physiological properties in detailed compartmental simulations is an important step in investigating their role in network dynamics.

FIGURE 7. Simulation of subthreshold membrane potential oscillations in a more detailed simulation containing a wider range of membrane currents in addition to the two currents used in the simplified representation. **A:** These additional currents do not prevent the appearance of subthreshold membrane potential oscillations. For increased current amplitudes (0.0, 0.02, 0.05, 0.07, 0.082 nA, respectively), the oscillation amplitude increases. The frequency for the top three traces is 9–12 Hz. **B:** Transition from single spiking to clustering and finally tonic firing. Increased current stimulation from top to bottom 0.078 nA, 0.083 nA and 0.098 nA, respectively. **C:** Rebound spike following termination of a hyperpolarizing current injection of -0.12 nA. The sag% is 28%, close to the experimentally reported value for sharp electrodes of 30% (Alonso and Klink 1993). The dash-dotted line shows a cell with all the I_h -current set to the fast component. The dashed line shows all currents on the slow component. With only a fast component, a rebound produces a spike followed by a hyperpolarization. With only a slow time constant, two spikes are produced, followed by an increased depolarization, indicating the potential role of the slow component in clustering.

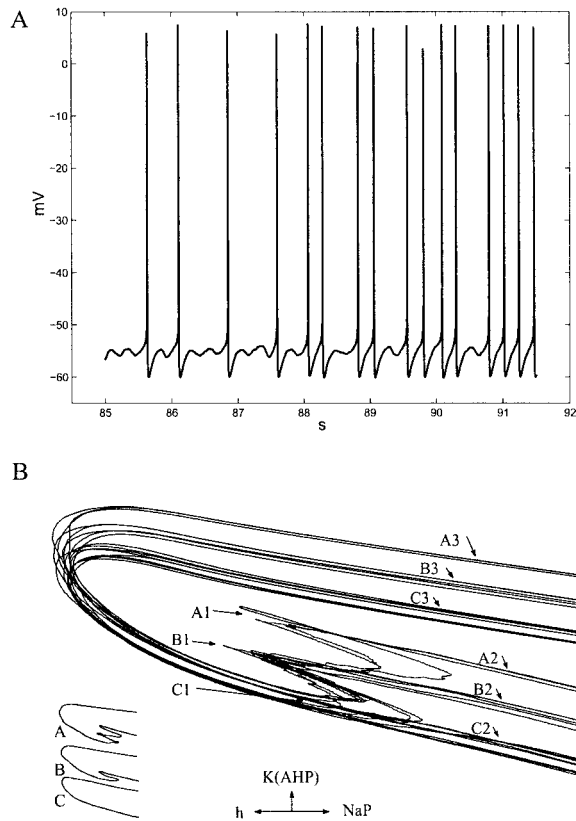


FIGURE 8. Phase plane plot of clustering in the full model. **A:** Soma membrane potential is plotted versus time. During simulation, the current is increased linearly. Single spikes are separated by one or two cycles of oscillations, cluster doublets and multiplets are also shown. **B:** Phase plane plot of currents during the simulation in 8A. I_h , I_{NaP} , and $I_{K(AHP)}$ currents. The view is a plane projection along the diagonal of the I_h - I_{NaP} plane (i.e., as axes indicate along constant $I_{K(AHP)}$ and with I_{NaP} increasing to the right and I_h to the left). There are three different families of trajectories for a spike, depending on whether it is preceded by two (A), one (B), or no (C) oscillations. As can be seen, they are primarily separated along the $I_{K(AHP)}$ -axis indicating that the time evolution of clusters and oscillations depends on decay of spike associated Ca-influx affecting $I_{K(AHP)}$. In the inset the three classes of trajectories are drawn schematically. A trajectory starts at 1 and goes to 2, 3, and then repeats; 1 represents the subthreshold oscillation portion, 2 the rising, and 3 the falling part of a spike.

Oscillation Characteristics

A number of factors contribute to the size of the amplitude and the frequency of the subthreshold oscillations. First, a match between the cell membrane time constant (cell resonance frequency) and the oscillation frequency is important. Second, it is important that all compartments have a sizable conductance for I_h and I_{NaP} in order to participate in the membrane oscillation. Third, the slope of the activation curves of I_h and I_{NaP} determines the amplitude of the current difference (between peaks and troughs) during the oscillation in membrane potential. This affects the oscillation amplitude and frequency. Fourth, the h -current time constant, mainly I_h (fast), affects the oscillation frequency. Fifth, oscillation frequency increases with increased conductance of I_h and I_{NaP} .

In experiments, the oscillation amplitude decreases above -55 mV. In the model, however, the amplitude decreases at a point that

was 4 mV more depolarized. This difference may result from depolarization activating an additional outward rectifying potassium current in the cell, which is lacking in the model. Alternatively, the Na current of the model may activate at a somewhat too hyperpolarized level.

In the simulations, as well as in experiments (Alonso and Klink, 1993) (Fig. 4A), the oscillations frequently are asymmetric, as noted in conjunction with Figure 2C. Typically, the rising phase shows a smaller slope than the falling phase. This can be explained by the difference in net current change between the rising phase and the falling phase which originates in the difference between I_h activation rate constants α and deactivation rate constants β . This variation in current is amplified by I_{NaP} , and the amplification factor depends on the slope of the activation curve of I_{NaP} .

Oscillations appear as a relatively robust phenomenon in the model. During this research, a number of variations of parameter values have been performed. Variations have included parameters controlling electrotonic length, compartment structure, input resistance, soma membrane time constant and conductance profile (specifically for I_h and I_{NaP}). Further, the shape of the steady-state activation curve and the activation time constant curves were varied, in addition to explorations of the effect of using one versus two steady-state activation curves. In most of these cases, oscillations were still obtained in the simulations. Overall, the oscillations were most sensitive to the balance between conductances g_h and g_{NaP} and the rate of change of I_h and I_{NaP} (the derivative of the steady-state activation curve) in the oscillation interval. In some cases, quite large oscillation amplitudes were obtained (≤ 5 mV). However, these cases were rather sensitive to changes in the current and conductance balance of the cell. For more moderate amplitudes, like those presented in Figures 2, 3, 5, 7, 8, the amplitudes were much more consistent. The oscillation amplitude and frequency appeared over a narrower range in the model than in the real cell. An interesting observation is that the oscillation depends on a difference between time constants of I_h and I_{NaP} ; if the two are equal, oscillations do not develop.

Stable oscillations can be obtained within a limited parameter range without the need for adding noise to the simulation (data not shown). (See also the one-compartment model of Dickson et al., 2000.) This is primarily of theoretical interest because it shows that not only fixed point, but limit cycles (oscillations), exist as (numerical) solutions to the equations for I_h and I_{NaP} . Stable oscillations also exist in a wider parameter interval if noise is present. This is of more practical interest, as noise is present in real tissue, and the oscillations are facilitated by it. This also reduces the model's sensitivity to variations in parameter values. The source of this noise is unknown. White et al. (1998) argued that NaP-channel noise could be the source. Noise could also come from a noisy cation current (Shalinsky et al., 2002). In vivo, this channel noise may be rather small compared to synaptic noise, but the experimental data show oscillations in the presence of synaptic blockers (Dickson et al., 2000). The oscillations are not dependent on the particular amplitude or frequency of this noise. Additionally, by adding noise to the simulations, one also avoids the risk of a simulation result, depending on a very specific set or sequence of state variables. The fast component is the main source of the oscilla-

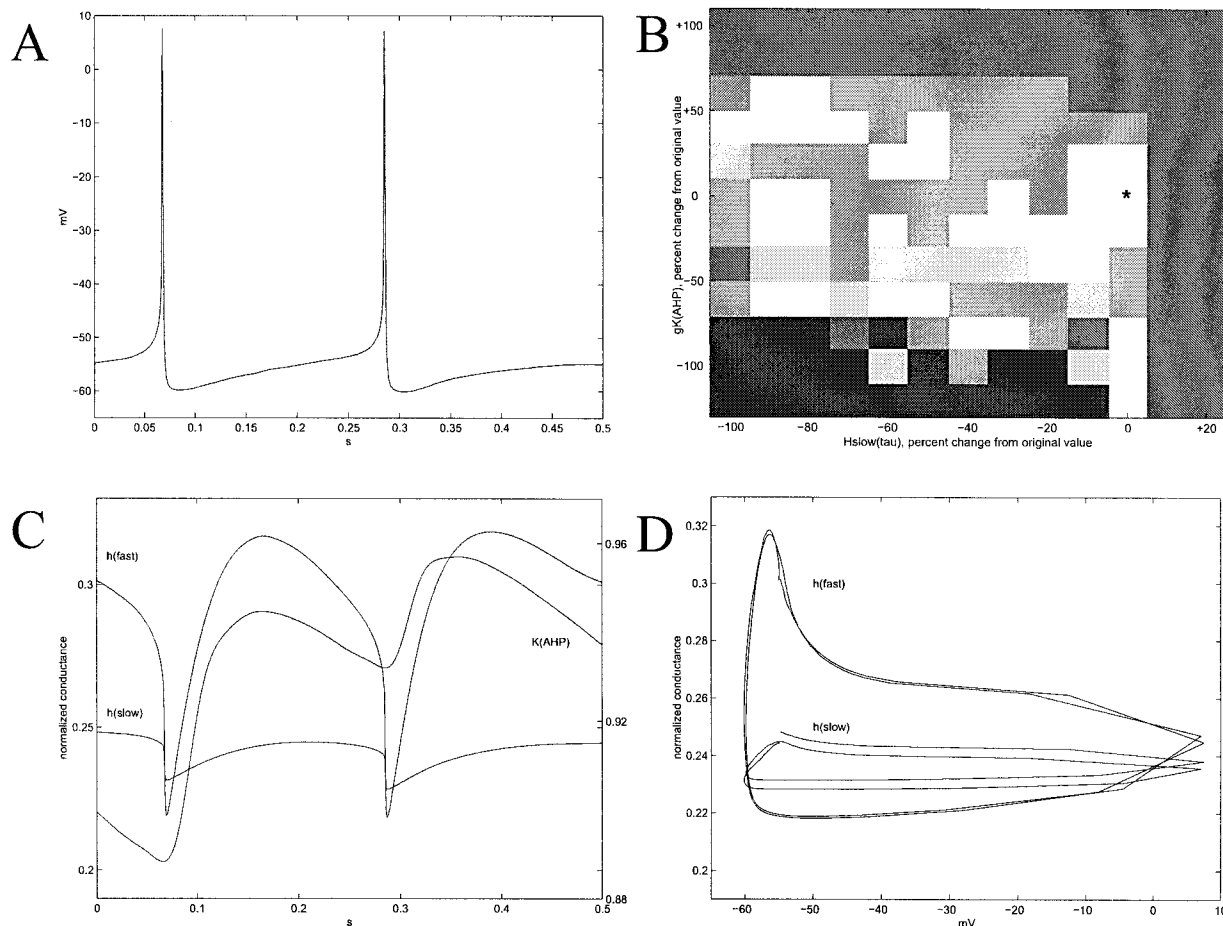


FIGURE 9. Full model, analysis of the generation of clustering due to $I_{K(AHP)}$ and I_h . The same data are plotted in A, C, and D to permit comparisons of time and conductance dependence. B: Separate study of $I_{K(AHP)}$ and I_h . Both the $I_{K(AHP)}$ and the slow component of I_h contribute to clustering. A: Plot of simulated membrane potential showing two consecutive spikes in a cluster (doublet) during spiking induced by current injection. After the second spike, there is a much longer delay before generation of another spike (not shown). B: To investigate the role of the slow component further, together with the role of the $K(AHP)$ current, a variation in conductance of $I_{K(AHP)}$ and variation in time constant of the slow component of I_h was conducted. The original value of $I_{K(AHP)}$ and the slow component of I_h is indicated by an asterisk (*). These two components enclose a region of robust clustering. Note that every point corresponds to a full run with a linearly increased current ramp. The firing was then classified according to the following: black: only tonic firing, dark gray: only single spikes with oscillations between as well as tonic firing, medium gray: doublets and single spikes and tonic firing, light gray: triplets and single spikes and tonic firing, white: doublets, triplets, single spiking and tonic firing. The value for $I_{K(AHP)}$ is percentage change from original value (-100 means $I_{K(AHP)} = 0$, $+100$ means a doubling of $I_{K(AHP)}$). The value for I_h slow time constant was varied by fixing the peak of the curve and compressing or expanding the curve along the time constant axis, with the multiplicative factor (in

percentage change from original value) indicated. This means that -100 corresponds to a constant value at the peak 390 ms, -50 corresponds to the tails of the curve only reaching halfway down to the control value. (For increases, i.e., values above 0, a lower limit of 1 ms was used.) C: Normalized conductance of the fast and slow components of I_h as well as $I_{K(AHP)}$ are plotted versus time to show how these conductances change in relation to the membrane potential plot shown in A. (To see how currents develop over time, see also Fig. 6B.) Left scale shows magnitude of conductance of I_h fast and slow, while right scale shows magnitude of conductance of $I_{K(AHP)}$. Note the clear increase in $I_{K(AHP)}$ with the second spike. Decreases in $h(\text{slow})$ are shown in D. D: Fast (larger orbit) and the slow component's normalized conductances (smaller orbit) are plotted versus membrane potential (-60 to $+10$ mV). Relation to time can be seen in C. As shown in the larger orbit, the two cycles are almost superimposed, indicating that the fast component does not change significantly between the two spikes, i.e., it does not contribute to making a difference between the first and the second spike. The slow component, in contrast, decreases (shifts downward) between the two spikes. The reduction of the slow component is 6.4 times larger than the reduction of the fast component, indicating that reduction in the depolarization caused by deactivation of the slow component of the current may contribute to the clustering.

tions together with I_{NaP} , as shown in Figures 6A and 7C, and also demonstrated by the absence of oscillations in the absence of a fast component of I_h . As shown in Figures 6A and 7C, as well as the absence of oscillations in the absence of a fast component of I_h , the fast component is the main source of the oscillations together with I_{NaP} .

Fast and Medium Afterhyperpolarizations

With regard to the modeling of the mAHP in Figure 6B and modeling of spike clustering phenomena, the I_h time constants are not known for voltages greater than -40 mV, but the action

potentials go well beyond this value. Therefore, the size of the I_h time constants during the spike are not known. In any event, it seems clear that I_h does not have time to close fully during the spike (Spain et al., 1987). Consistent with this possibility is the observation that blocking of I_h with ZD7288 affects the shape of the spike and the subsequent mAHP. If some degree of current remains during the spike, the period after the spike will be affected, and thus the membrane will retain a sort of memory for the last spike, as indicated in Figure 7C. Because of this, I_h may also influence phenomena such as spike clustering.

The relatively shallow fAHPs of SCs may be due to h-current activation during the repolarization. Further, a better fit to the shallow fAHPs in the experimental data was obtained when the simulations included an initial segment compartment. In addition to this influence, inclusion of the initial segment also gave a better fit for the action potential and spike frequency adaptation, as in other work (Ekeberg et al., 1991; Traub et al., 1994; Driesang and Pape 1997).

Clustering

A number of factors may contribute to the phenomenon of clustering. The calcium-dependent potassium current KAHP appears to play an important role in causing clustering. An additional source of clustering may be the noisy properties of the Na channel, as suggested by White et al. (1998). In experiments as well as in these simulations, reduction of calcium influx strongly reduces the clustering tendency (Klink and Alonso, 1993), which is understandable, since KAHP activation counteracts repeated spiking. As shown in Figure 9B, $I_{K(AHP)}$, plays a key role in clustering together with the slow component of I_h . Spiking leads to Ca-influx that activates the Ca-sensitive $I_{K(AHP)}$ and the depolarized potential levels during the spike lead to deactivation of the slow component of I_h . As shown in Figure 9, the region of parameters producing a full range of features, oscillations, single spikes, clustering, and tonic firing is quite extended. This analysis indicates the region of existence of these physiological components. The region in which these are produced frequently and robustly is smaller, but it also shows robustness for the parameters. The operating point for clustering that was found for the slow time constant of I_h and for the conductance of $I_{K(AHP)}$ is rather close to the border of the I_h time constant scaling value of +5 beyond which only single spikes are seen. This is a common feature in control theory, where systems are located close to the boundary (but with some safety margin) to facilitate rapid state transitions.

In conclusion, clustering might depend on two components, one depolarizing on a shorter time scale, and one hyperpolarizing on a longer time scale. I_h rebound after the fAHP could contribute to the first component, and subsequent KAHP and I_h (slow) activation to the second component.

Space Clamp

The uniform distribution of I_h in this modeled neuron is an assumption. In CA1 pyramidal cells, there is a high distal density of I_h , as shown by immunohistochemistry (Santoro et al., 1997) and electrophysiology (Magee, 1998). In the voltage-clamp recordings, the current does not undergo the immediate step increase which

would be expected in response to the voltage step starting from a potential which gives a conducting state of I_h . Instead, the current increase shows a finite slope during the initial rise in response to the voltage step. In the model, an increased density of I_h in the distal portions of the dendrite gave an overall better fit to this portion of the voltage-clamp data (data not shown). The possibility of space clamp affecting a sizable I_h current at distal locations is further supported by the fact that a version of the cell model with larger dendritic attenuation (longer and thinner compartments) gave further improved fit to the experimental data (data not shown).

Apart from this effect on the rising phase of the current, would a distal location of I_h lead to incorrect results due to dendritic filtering? Previous research suggests that spatial segregation of channels from recording should not have a large effect on the determination of reversal potential (Spruston et al., 1993). Neither should this segregation affect the channel kinetics, which are rather slow for I_h (Spruston et al., 1993). There might be some minor effect on the steady-state activation curve due to differences in potential between the recording site and the potential at the site of the channels themselves. These would primarily affect slope, but might also affect the half-activation potential (Spruston et al., 1993). The passive delay of a distally generated I_h current due to the low-pass filtering of the dendrite may not be as large, however, in the model as in the real cell.

Role of I_{NaP} and I_h

Some properties of how I_{NaP} and I_h influence membrane potential changes have been observed during the simulation work. The derivative of the I_{NaP} steady-state activation curve controls the amplification of voltage fluctuations and hence the stability of the membrane potential (the risk of runaway depolarization leading to spikes). NaP current inactivation may stabilize the excitability of cells due to the inactivation during long periods of depolarization.

For the h-current, the steady-state activation had to be modeled quite accurately around the positive end. A regular Boltzmann approximation will overestimate the current in this region. This will then have to be compensated by a larger conductance for I_{NaP} . This will give an extra depolarizing bias current, which will change the resting potential or the input resistance. Further, the slope of the regular Boltzmann is not as large as the experimentally observed curve in this region. Use of the smaller slope of the regular Boltzmann would impair the generation of subthreshold oscillations in the simulation (data not shown).

The time constant of activation was best fitted with two exponentials. The amplitudes of these two components varied with voltage, with almost equal amplitudes around -60 mV and increasing relative size for the fast component on each side of this. To include this in the model, the steady-state function was split into two components. The effect of this within the oscillation potential interval is a small change in relative contribution of the fast component to the slow component, and a small change in the rate of change of the fast component.

In the present work, we have described how the two components of I_h may serve different roles in the activity displayed by the cell: the fast component in the generation of subthreshold oscillations, and the slow component in the generation of clusters. It is

also interesting to note the similarities in time constant of the two components of I_h when they exert their contribution. The fast component contributes primarily to oscillations, and in the oscillating regime the time constant is ~ 60 ms. The slow time constant contributes mostly to the clustering, and in the spiking regime (around -10 mV), the time constant is also 60 ms. This observation may be paralleled with the experimental data on the average frequency of subthreshold oscillations, 8.6 Hz, and the frequency of spikes within a cluster, commonly ~ 10 Hz.

Functional Implications

The factors influencing subthreshold MPOs may play an important role in the network dynamics of entorhinal cortex and its interactions with the hippocampal formation. Cholinergic modulation has a strong effect on inducing subthreshold oscillations in the slice (Klink and Alonso, 1993, 1997a,b) and also influences theta rhythm field potential oscillations in whole animal preparations (Alonso and Garcia-Austt, 1987). Cholinergic depolarization in the SCs is mediated by the activation of a “noisy” cation current, known as I_{NCM} (Shalinsky et al., 2002). This current has a quite slow kinetics and would not affect spike or oscillation properties, but NCM-channel noise could, as discussed above, promote the generation of more robust oscillations. The influence of currents underlying subthreshold oscillations could make the network resonate at theta frequency. The detailed single cell simulations containing these currents presented in this study will permit analysis of their role in network dynamics. SCs are rhythmically and strongly inhibited by layer I–II interneurons (Dickson and Alonso, 1997). The presence of I_h not only enables the cell to show subthreshold membrane oscillations, but also to give a rebound spike in response to a hyperpolarizing input. In consequence, if a population of oscillating SCs is inhibited simultaneously, they will respond to this input by synchronizing their activities through a “reset” phenomenon implemented by I_h .

The relative timing of neuronal activity within the entorhinal cortex and hippocampus could be very important to the functional interaction of these regions. Different cell types show preferential activity during different phases of theta in both hippocampus (Fox et al., 1986; Skaggs and McNaughton, 1996), and entorhinal cortex (Alonso and Garcia-Austt, 1987). This may allow afferent input to arrive in the hippocampus at a particular phase relative to intrinsic dynamics. In particular, it has been suggested that alternating phases of dominant afferent input and intrinsic excitatory spread may enhance the encoding and retrieval of activity sequences within the hippocampal formation (Wallenstein and Hasselmo, 1997; Sohal and Hasselmo, 1998). In network simulations of potential mechanisms of episodic memory function of the hippocampal formation, phasic changes in neuronal activity prove important for terminating prior retrieval activity during the initiation of a new retrieval cycle (Hasselmo and Wyble, 1997; Hasselmo et al., 2002).

Acknowledgments

The authors thank Clara Bodelón for discussions on analysis of nonlinear systems.

NOTE ADDED IN PROOF

In a recent experimental HCN1 knockout study in entorhinal cortex (Nolan et al., 2003), several of the conclusions in this work were supported. The current studied had a biphasic kinetics as the one in our study. In the knockout, sag was absent, as well as subthreshold oscillations, and spike clustering was affected.

REFERENCES

- Acker CD, Haas JS, Kopell N, White JA. 2001. Predicting synchrony in the oscillatory stellate cells of the entorhinal cortex. *Soc Neurosci Abs* 27:47.3.
- Alonso AA, Garcia-Austt E. 1987. Neuronal sources of theta rhythm in the entorhinal cortex of the rat. II. Phase relations between unit discharges and theta field potentials. *Exp Brain Res* 67:502–509.
- Alonso AA, Kohler C. 1984. A study of the reciprocal connections between the septum and the entorhinal area using anterograde and retrograde axonal transport methods in the rat brain. *J Comp Neurol* 225:327–343.
- Alonso AA, Llinas RR. 1989. Subthreshold Na^+ -dependent theta-like rhythmicity in stellate cells of entorhinal cortex layer II. *Nature* 342:175–117.
- Alonso AA, Klink R. 1993. Differential electroresponsiveness of stellate and pyramidal-like cells of medial entorhinal cortex layer II. *J Neurophysiol* 70:128–143.
- Alonso AA, Magistretti J. 1998. Biophysical properties and slow inactivation of a sustained Na^+ current in layer II stellate cells (SCs) of rat entorhinal cortex. *Soc Neurosci Abs* 24: 814.4.
- Baker K, Warren KS, Yellen G, Fishman MC. 1997. Defective “pacemaker” current (I_h) in a zebrafish mutant with a slow heart rate. *Proc Natl Acad Sci USA* 94:4554–4559.
- Bower JM, Beeman D. 1995. The book of GENESIS: exploring realistic neural models with the GENeral NEural SIMulation System. New York: Springer-Verlag.
- Brunel N, Hakim V, Richardson MJE. 2001. Analysis of resonance properties of neuronal models. *Soc Neurosci Abs* 27:47.6.
- DeSchutter E, Bower JM. 1994. An active membrane model of the cerebellar purkinje cell. I. Simulation of current clamps in slice. *J Neurophysiol* 71:375–400.
- Dickson CT, Alonso AA. 1997. Muscarinic induction of synchronous population activity in the entorhinal cortex. *J Neurosci* 17:6729–6744.
- Dickson CT, Alonso AA. 1998. Role of I_h in the generation of subthreshold membrane potential oscillations (MPOs) of entorhinal cortex (EC) layer II stellate cells. *Soc Neurosci Abs* 24:814.3.
- Dickson CT, Magistretti J, Shalinsky MH, Fransén E, Hasselmo ME, Alonso AA. 2000. Properties and role of I_h in the pacing of subthreshold oscillations in entorhinal cortex layer II neurons. *J Neurophysiol* 83:2562–2579.
- DiFrancesco D, Ferroni M, Mazzanti M, Tromba C. 1986. Properties of the hyperpolarizing activated current (I_f) in cells isolated from the rabbit sino-atrial node. *J Physiol* 377:61–88.
- Driesang RB, Pape HC. 1997. Generation of spike doublets in projection neurons of the lateral amygdala: mechanisms and significance for rhythmic spike firing. *Soc Neurosci Abs* 23:891.5.
- Ekeberg Ö, Wallén P, Lansner A, Tråvén H, Brodin L, Grillner S. 1991. A computer based model for realistic simulations of neural networks. I. The single neuron and synaptic interaction. *Biol Cybern* 65:81–90.
- Erchova IA, Kreck G, Muller R, Herz A. 2001. Modeling subthreshold frequency profiles of stellate cells in the entorhinal cortex. *Soc Neurosci Abs* 27:47.8.

- Fox SE, Wolfson S, Ranck JBJ. 1986. Hippocampal theta rhythm and the firing of neurons in walking and urethane anesthetized rats. *Exp Brain Res* 62:495–508.
- Fransén E, Dickson CT, Magistretti J, Alonso AA, Hasselmo ME. 1998. Modeling the generation of subthreshold membrane potential oscillations of entorhinal cortex layer II stellate cells. *Soc Neurosci Abs* 24: 814.5.
- Fransén E, Wallenstein GV, Alonso AA, Dickson CT, Hasselmo ME. 1999. A biophysical simulation of intrinsic and network properties of entorhinal cortex. *Neurocomputing* 26/27:375–380.
- Gutfreund Y, Yarom Y, Segev I. 1995. Subthreshold oscillations and resonant frequency in guinea pig cortical neurons: physiology and modeling. *J Physiol* 483.3:621–640.
- Hasselmo ME, Wyble BP. 1997. Simulation of the effects of scopolamine on free recall and recognition in a network model of the hippocampus. *Behav Brain Res* 89:1–34.
- Hasselmo ME, Bodelón C, Wyble BP. 2002. A proposed function for hippocampal theta rhythm: separate phases of encoding and retrieval enhance reversal of prior learning. *Neural Comput* 14:793–817.
- Hodgkin AL, Huxley AF. 1952. A quantitative description of membrane current and its application to conduction and excitation in nerve. *J Physiol* 117:500–544.
- Huguenard JR, McCormick DA. 1992. Simulation of the currents involved in rhythmic oscillations in thalamic relay neurons. *J Neurophysiol* 68:1373–1383.
- Hutcheon B, Miura RM, Puil E. 1996a. Models of subthreshold membrane resonance in neocortical neurons. *J Neurophysiol* 76:698–714.
- Hutcheon B, Miura RM, Puil E. 1996b. Subthreshold membrane resonance in neocortical neurons. *J Neurophysiol* 76:683–697.
- Klink R, Alonso AA. 1993. Ionic mechanisms for the subthreshold oscillations and differential electroresponsiveness of medial entorhinal cortex layer II neurons. *J Neurophysiol* 70:144–157.
- Klink R, Alonso A. 1997a. Muscarinic modulation of the oscillatory and repetitive firing properties of entorhinal cortex layer II neurons. *J Neurophysiol* 77:1813–1828.
- Klink R, Alonso AA. 1997b. Ionic mechanisms of muscarinic depolarization in entorhinal cortex layer II neurons. *J Neurophysiol* 77:1829–1843.
- Klink R, Alonso AA. 1997c. Morphological characteristics of layer II projection neurons in the rat medial entorhinal cortex. *Hippocampus* 7:571–583.
- Llinas R, Jahnsen H. 1982. Electrophysiology of mammalian thalamic neurons in vitro. *Nature* 297:406–408.
- Llinas R, Yarom Y. 1986. Oscillatory properties of guinea-pig inferior olivary neurones and their pharmacological modulation: an in vitro study. *J Physiol* 376:163–82.
- Ludwig A, Zong X, Jeglitsch M, Hofmann F, Biel M. 1998. A family of hyperpolarization-activated mammalian cation channels. *Nature* 393: 587–591.
- Magee JC. 1998. Dendritic hyperpolarization-activated currents modify the integrative properties of hippocampal CA1 pyramidal neurons. *J Neurosci* 18:7613–7624.
- Magistretti J, Alonso AA. 1999. Biophysical properties and slow voltage-dependent inactivation of a sustained sodium current in entorhinal cortex layer-II principal cells: a whole-cell and single-channel study. *J Gen Physiol* 114:491–509.
- Magistretti J, Ragsdale D, Alonso AA. 1999a. Direct demonstration of persistent Na⁺ channel activity in dendritic processes of mammalian cortical neurones. *J Physiol* 521:629–636.
- Magistretti J, Ragsdale D, Alonso AA. 1999b. High conductance sustained single channel activity responsible for the low threshold persistent Na current in entorhinal cortex neurons. *J Neurosci* 19:7334–7341.
- McCormick DA, Pape HC. 1990. Properties of a hyperpolarization-activated cation current and its role in rhythmic oscillations in thalamic relay neurons. *J Physiol* 431:291–318.
- McCormick DA, Huguenard JR. 1992. A model of the electrophysiological properties of thalamocortical relay neurons. *J Neurophysiol* 68: 1384–1400.
- Nolan MF, Santoro B, Morozov A, Siegelbaum SA, Kandel ER. 2003. Contribution of HCN1 to membrane properties and intrinsic oscillations of layer II neurons from the entorhinal cortex. *Prog. No.* 171.11. 2003 Abst. Viewer/Itinerary Planner. Washington, DC: Society for Neuroscience, Online.
- Pape HC. 1996. Queer current and pacemaker: the hyperpolarization-activated cation current in neurons. *Annu Rev Physiol* 58:299–327.
- Pape HC, Pare D, Driesang RB. 1998. Two types of intrinsic oscillations in neurons of the lateral and basolateral nuclei of the amygdala. *J Neurophysiol* 79:205–216.
- Robinson RB, Siegelbaum SA. 2003. Hyperpolarization-activated cation currents: from molecules to physiological function. *Annu Rev Physiol* 65:453–80.
- Santoro B, Grant SGN, Bartsch D, Kandel ER. 1997. Interactive cloning with the SH3 domain of N-src identifies a new brain specific ion channel protein, with homology to Eag and cyclic nucleotide gated channels. *Proc Natl Acad Sci USA* 94:14815–14820.
- Santoro B, Liu DT, Yao H, Bartsch D, Kandel ER, Siegelbaum SA, Tibbs GR. 1998. Identification of a gene encoding a hyperpolarization-activated pacemaker channel of brain. *Cell* 93:717–729.
- Santoro B, Chen S, Luthi A, Pavlidis P, Shumyatsky GP, Tibbs GR, Siegelbaum SA. 2000. Molecular and functional heterogeneity of hyperpolarization-activated pacemaker channels in the mouse CNS. *J Neurosci* 20:5264–5275.
- Shalinsky MH, Magistretti J, Ma L, Alonso AA. 2002. Muscarinic activation of a cation current and associated current noise in entorhinal-cortex layer-II neurons. *J Neurophysiol* 88:1197–1211.
- Skaggs WE, McNaughton BL. 1996. Replay of neuronal firing sequences in rat hippocampus during sleep following spatial experience. *Science* 271:1870–1873.
- Sohal VS, Hasselmo ME. 1998. GABA_B modulation improves sequence disambiguation in computational models of hippocampal region CA3. *Hippocampus* 8:171–193.
- Spain WJ, Schwandt PC, Crill WE. 1987. Anomalous rectification in neurons from cat sensorimotor cortex in vitro. *J Neurophysiol* 57:1555–1576.
- Spruston N, Jaffe DB, Williams SH, Johnston D. 1993. Voltage- and space-clamp errors associated with the measurement of electrotonically remote synaptic events. *J Neurophysiol* 70:781–802.
- Traub RD, Wong RKS, Miles R, Michelson H. 1991. A model of a CA3 pyramidal neuron incorporating voltage-clamp data on intrinsic conductances. *J Neurophysiol* 66:635–650.
- Traub RD, Jefferys JG, Miles RM, Whittington MA, Toth K. 1994. A branching dendritic model of a rodent CA3 pyramidal neurone. *J Physiol* 481:79–95.
- Vasilyev DV, Barish ME. 2002. Postnatal development of the hyperpolarization-activated excitatory current ih in mouse hippocampal pyramidal neurons. *J Neurosci* 22:8992–9004.
- Wallenstein GV, Hasselmo ME. 1997. GABAergic modulation of hippocampal population activity. Sequence learning, place field development and the phase precession effect. *J Neurophysiol* 78:393–408.
- Wang XJ. 1993. Ionic basis for intrinsic 40 Hz neuronal oscillations. *NeuroReport* 5:221–224.
- White JA, Budde T, Kay AR. 1995. A bifurcation analysis of neuronal subthreshold oscillations. *Biophys J* 69:1203–1217.
- White JA, Klink R, Alonso AA, Kay AR. 1998. Noise from voltage-gated ion channels may influence neuronal dynamics in the entorhinal cortex. *J Neurophysiol* 80:262–269.
- Williams SR, Turner JP, Hughes SW, Crunelli V. 1997. On the nature of anomalous rectification in thalamocortical neurons of the cat ventrobasal thalamus in vitro. *J Physiol* 505:727–747.
- Young BJ, Otto T, Fox GD, Eichenbaum H. 1997. Memory representation within the parahippocampal region. *J Neurosci* 17:5183–5195.

APPENDIX

IONIC CURRENTS

Voltage-dependent conductances were modeled using a Hodgkin-Huxley type of kinetic model. Reversal potentials were for Na^+ + 87 mV, K^+ - 83 mV, and Ca^{2+} + 80 mV. The Na^+ current responsible for the fast action potentials had a kinetics taken from a model of hippocampal pyramidal cells (Traub et al., 1991, 1994). Both the Na as well as the K current were shifted +5 mV to make the spiking threshold more positive, around -50 mV. The spatial distribution and maximal conductance of all currents on the different compartments are found in Table 2. The maximal conductances were adjusted to match the action potential rate of depolarization (Na^+) and rate of repolarization (K^+), as well as spike threshold, amplitude, and duration (Na^+ and K^+) of experimental data (Alonso and Klink, 1993).

Na

$$\alpha_m(V) = \frac{320 \cdot 10^3(0.0131 - V)}{\exp[(0.0131 - V)/0.004] - 1}$$

$$\beta_m(V) = \frac{280 \cdot 10^3(V - 0.0401)}{\exp[(V - 0.0401)/0.005] - 1}$$

$$\alpha_h(V) = 128 \exp[(0.017 - V)/0.018]$$

$$\beta_h(V) = \frac{4 \cdot 10^3}{1 + \exp[(0.040 - V)/0.005]}$$

 K_{dr}

$$\alpha_m(V) = \frac{16 \cdot 10^3(0.0351 - V)}{\exp[(0.0351 - V)/0.005] - 1}$$

$$\beta_m(V) = 250 \exp[(0.020 - V)/0.040]$$

 Ca_I

The high-threshold Ca^{2+} current was modeled according to Traub et al. (1994). The maximal conductance was set to the same value as in Traub et al. (1994).

$$\alpha_m(V) = \frac{1.6 \cdot 10^3}{1 + \exp[-72(V - 0.065)]}$$

$$\beta_m(V) = \frac{20 \cdot 10^3(V - 0.0511)}{\exp[(V - 0.0511)/0.005] - 1}$$

 K_{AHP}

The calcium-dependent K^+ (afterhyperpolarization) current was modeled according to Traub et al. (1991), with the slope 6.0

and the saturation 30 (arbitrary units). The maximal conductance was adjusted to match the sAHP depth (Alonso and Klink, 1993).

$$\alpha_m([\text{Ca}^{2+}]) = \min(6.0 \cdot [\text{Ca}^{2+}], 30)$$

$$\beta_m = 1.0$$

 K_C

The fast calcium- and voltage-dependent K^+ current was modeled according to Traub et al. (1991). The maximal conductance was adjusted to match the fAHP depth, and Ca-dependent spike repolarization rate (Alonso and Klink, 1993).

$$V \leq 0.050$$

$$\alpha_m(V) = \frac{\exp(53.872V - 0.66835)}{0.018975}$$

$$\beta_m(V) = 2000\{\exp[(0.0065 - V)/0.027]\} - \alpha_m$$

$$V > 0.050$$

$$\alpha_m(V) = 2000\{\exp[(0.0065 - V)/0.027]\}$$

$$\beta_m(V) = 0$$

CAN

The nonspecific Ca^{2+} -dependent cationic current was modeled similarly to the calcium-dependent K^+ current found in Traub et al. (1991). The maximal conductance was adjusted to match the depolarization following carbachol application (Klink and Alonso, 1997a,b).

$$\alpha_m([\text{Ca}^{2+}]) = \min(0.02 \cdot [\text{Ca}^{2+}], 10)$$

$$\beta_m = 1.0$$

 Ca^{2+} BUFFERING

The Ca^{2+} diffusion and buffering was modeled according to Traub et al. (1991) and McCormick and Huguenard (1992). To take into account the differences in distances and diffusion constants for the calcium related to the different currents, the calcium kinetics was modeled separately for each case. For the calcium related to the calcium-dependent K^+ current, the diffusion rate constant of 0.2 s was set to give the spike frequency adaptation rate according to Alonso and Klink (1993). The conversion factor, ϕ , from charge density to concentration for each compartment is found in Table 2, and the minimal $[\text{Ca}^{2+}]_i$ was set to $5.0 \cdot 10^{-3}$. For the fast calcium- and voltage-dependent K^+ current, the calcium values were 0.5 ms, $17.402 \cdot 10^{12}$, and $5.0 \cdot 10^{-6}$, respectively, and the related values for the nonspecific Ca^{2+} -dependent cationic current were 0.133s, $17.402 \cdot 10^{11}$, and $5.0 \cdot 10^{-3}$, respectively.